

Contents

1	Introduction and Theory Overview	1
1.1	Introduction	1
1.2	Theory Overview	2
1.2.1	Heavy Vector Triplet Model	2
1.2.2	Basic Phenomenology	3
1.2.3	Explicit Models	8
2	CMS detector and LHC	11
2.1	Large Hadron Collider	11
2.2	Compact Muon Solenoid	13
2.2.1	Tracker	15
2.2.2	ECAL	16
2.2.3	HCAL	17
2.2.4	Muon Chamber	19
2.2.5	Trigger System	20
3	Analysis Procedures	22
3.1	Monte Carlo Samples and Data sets	22
3.1.1	Signal MC	22
3.1.2	Background MC	24
3.1.3	Data Samples	24
3.2	Trigger	25
3.3	Physics Objects	26

3.3.1	Muon	26
3.3.2	Electron	28

List of Figures

1-1	Branching ratios as a function of the resonance mass for the HVT benchmark model A(left) and model B(right).	10
1-2	Theoretical production cross-section as a function of new resonance particles for HVT model B benchmark. Dash lines are 8 TeV predictions while solid lines are 13 TeV predictions.	10
2-1	Overview of the LHC and relative location of the detectors.	12
2-2	CERN accelerator complex.	13
2-3	Structure overview of the CMS detector.	14
2-4	Schematic layout of tracker.	15
2-5	The pixel detector inside tracker.	15
2-6	Schematic layout of the CMS ECAL.	17
2-7	Longitudinal view of one quarter of CMS and the location of HB (hadron barrel calorimeter), HE (hadron endcap calorimeter), HF (hadron forward calorimeter) and HO (hadron outer calorimeter)	18
2-8	Slice view of one quarter of muon chamber system.	20
2-9	CMS triggering and data acquisition architecture.	21
3-1	Feynman diagram for $Z' \rightarrow Zh \rightarrow 2l2q$	23

List of Tables

3.1	Signal samples used in the analysis.	23
3.2	Background samples used in the analysis.	24
3.3	Data sets used in this analysis.	25
3.4	Summary of the muon ID selection criteria.	28

¹ Chapter 1

² Introduction and Theory Overview

³ 1.1 Introduction

⁴ This thesis presents the analysis details and the results of the search for heavy reso-
⁵ nances decaying into a Z boson and a Higgs boson (h) at the center-of-mass energy of
⁶ 8 TeV, using 19.7 fb^{-1} p-p collision data. In turn, the Z boson is identified through
⁷ its leptonic decays (leptons often refer to e and μ only in experiments. $l = e, \mu$). The
⁸ Higgs boson h is expected to hadronically decay into a pair of b-quarks. The investi-
⁹ gated final states consist of two charged leptons which are identified in the detector
¹⁰ and limit the presence of the background, and two b-quarks from the hadronic Higgs
¹¹ decay which collects the largest possible fraction of Higgs events.

¹² This thesis is organised as follows. In the latter part of this chapter, the model that
¹³ predicts heavy resonances is introduced, including the expected cross section and the
¹⁴ specification of model parameters. In chapter 2, the LHC and the CMS experiment
¹⁵ are described, including the information of each sub-detector and the trigger system
¹⁶ of the CMS. The details of the analysis are shown in chapter 3. This chapter reveals
¹⁷ the way to reconstruct physical objects in CMS. By adding some proper kinematic
¹⁸ selections on those physics objects, the interested events in data collected by the CMS
¹⁹ detector can be selected. Moreover, this chapter shows the comparison between data
²⁰ and simulation. In the last chapter, the results of the search and the conclusion are
²¹ presented.

22 1.2 Theory Overview

23 Although the Higgs boson discovered by the ATLAS and CMS collaborations [1–3]
 24 imposes strong constraints on theories beyond the Standard Model(SM), the extreme
 25 fine tuning in quantum corrections required to have a light fundamental Higgs boson
 26 with mass close to 125 GeV [4–7] suggests that the Standard Model may be incom-
 27 plete, and not valid beyond a scale of a few TeV. Various dynamical electroweak
 28 symmetry breaking scenarios which attempt to solve this naturalness problem, such
 29 as Minimal Walking Technicolor [8], Little Higgs [9–11], or composite Higgs mod-
 30 els [12–14] predict the existence of new resonances decaying to a vector boson plus a
 31 Higgs boson.

32 1.2.1 Heavy Vector Triplet Model

33 Resonance searches are typically not sensitive to all the details and the free parameters
 34 of the underlying model, but only to those parameters or combinations of parameters
 35 that control the mass of the resonance and the interactions involved in its production
 36 and decay. Therefore, one can employ a simplified description of the resonance de-
 37 fined by a phenomenological Lagrangian where only the relevant couplings and mass
 38 parameters are retained. This model-independent strategy applies a Heavy Vector
 39 Triplet (HVT) [15] to the Standard Model group and reproduces a large class of ex-
 40 plicit models. In Eq. (1.1), the mathematical form of the simplified Lagrangian is
 41 defined, where V_ν^a , $a = 1,2,3$, is a real vector with vanishing hypercharge in the ad-
 42 joint representation of $SU(2)_L$, it describes one charged and one neutral heavy spin-1
 43 particle with charge eigenstate fields, and $D_{[\mu} V_{\nu]}^a$ represents the covariant derivative.

$$\begin{aligned} \mathcal{L}_V = & -\frac{1}{4} D_{[\mu} V_{\nu]}^a D^{[\mu} V^{\nu]}_a + \frac{m_V^2}{2} V_\mu^a V^{\mu a} \\ & + ig_V c_H V_\mu^a H^\dagger \tau^a \overset{\leftrightarrow}{D}^\mu H + \frac{g^2}{g_V} c_F V_\mu^a \sum_f \bar{f}_L \gamma^\mu \tau^a f_L \\ & + \frac{g_V}{2} c_{VVV} \epsilon_{abc} V_\mu^a V_\nu^b D^{[\mu} V^{\nu]}_c + \text{quadrilinear terms} \end{aligned} \quad (1.1)$$

$$V_\mu^\pm = \frac{V_\mu^1 \mp i V_\mu^2}{\sqrt{2}}, \quad V_\mu^0 = V_\mu^3 \quad (1.2)$$

$$D_{[\mu} V_{\nu]}^a = D_\mu V_\nu^a - D_\nu V_\mu^a, \quad D_\mu V_\nu^a = \partial_\mu V_\nu^a + g \epsilon^{abc} W_\mu^b V_\nu^c \quad (1.3)$$

$$H = \begin{pmatrix} \phi^+ \\ \phi^- \end{pmatrix} = \begin{pmatrix} \frac{1}{\sqrt{2}}(\phi_1 + i\phi_2) \\ \frac{1}{\sqrt{2}}(\phi_3 + i\phi_4) \end{pmatrix} \quad (1.4)$$

⁴⁴

⁴⁵ In these models, new heavy vector bosons (V^\pm, V^0) that couple to the SM Higgs
⁴⁶ doublet (Eq. 1.4) and SM gauge bosons with the parameters c_H and g_V and to the
⁴⁷ fermions via the combination $(g^2/g_V)c_F$. The parameter g_V represents the strength
⁴⁸ of the new vector boson interaction, while c_H and c_F represent the couplings to the
⁴⁹ Higgs and the fermions respectively, and are expected to be of the order of unity in
⁵⁰ most models.

⁵¹ 1.2.2 Basic Phenomenology

⁵² Masses and Mixings

After electro-weak symmetry breaking (EWSB), the only massless state is photon, which can be identified as the gauge field associated with the unbroken $U(1)_{em}$. The two other neutral mass eigenstates are the SM Z boson and one heavy vector of mass M_0 which are obtained by diagonalizing the mass matrix of the (Z, V^0) system by a rotation with angle θ_N

$$\begin{pmatrix} Z \\ V^0 \end{pmatrix} \rightarrow \begin{pmatrix} \cos \theta_N & \sin \theta_N \\ -\sin \theta_N & \cos \theta_N \end{pmatrix} \begin{pmatrix} Z \\ V^0 \end{pmatrix}. \quad (1.5)$$

The mass matrix is

$$\mathcal{M}_N^2 = \begin{pmatrix} \hat{m}_Z^2 & c_H \xi \hat{m}_Z \hat{m}_V \\ c_H \xi \hat{m}_Z \hat{m}_V & \hat{m}_V^2 \end{pmatrix}, \text{ where } \begin{cases} \hat{m}_Z = \frac{e\hat{v}}{2\sin\theta_W \cos\theta_W} \\ \hat{m}_V^2 = m_V^2 + g_V^2 c_{VVHH} \hat{v}^2 \\ \xi = \frac{g_V \hat{v}}{2\hat{m}_V} \end{cases}. \quad (1.6)$$

In the above equations \hat{v} denotes the Vacuum Expectation Value (VEV) defined by $\langle H^\dagger H \rangle = \hat{v}^2/2$, and one should know the masses \hat{m}_Z and \hat{m}_V do not coincide with the physical Z boson and the masses of the new resonances of this model, although they do in the approximations later. The mass eigenvalues and the rotation angles are easily obtained by inverting the relations

$$\begin{aligned} Tr[\mathcal{M}_N^2] &= \hat{m}_Z^2 + \hat{m}_V^2 = m_Z^2 + M_0^2, \\ Det[\mathcal{M}_N^2] &= \hat{m}_Z^2 \hat{m}_V^2 (1 - c_H^2 \xi^2) = m_Z^2 M_0^2, \\ \tan 2\theta_N &= \frac{2c_H \xi \hat{m}_Z \hat{m}_V}{\hat{m}_V^2 - \hat{m}_Z^2}. \end{aligned} \quad (1.7)$$

⁵³ Notice that the tangent can be uniquely inverted because the angle θ_N is in the range

⁵⁴ $[-\pi/4, \pi/4]$ in the parameter region we will be interested in, where $\hat{m}_Z < \hat{m}_V$, and

⁵⁵ M_0 represents the real mass eigenvalue of the neutral heavy vector boson.

The situation is similar in the charged vector mass matrix of (W^\pm, V^\pm) system, and M_\pm denotes the real mass eigenvalue of charged states as well.

$$\mathcal{M}_C^2 = \begin{pmatrix} \hat{m}_W^2 & c_H \xi \hat{m}_W \hat{m}_V \\ c_H \xi \hat{m}_W \hat{m}_V & \hat{m}_V^2 \end{pmatrix}, \text{ where } \hat{m}_W = \frac{e\hat{v}}{2\sin\theta_W} = \cos\theta_W \hat{m}_Z, \quad (1.8)$$

where it is diagonalized by

$$\begin{aligned} Tr[\mathcal{M}_C^2] &= \hat{m}_W^2 + \hat{m}_V^2 = m_W^2 + M_\pm^2, \\ Det[\mathcal{M}_C^2] &= \hat{m}_W^2 \hat{m}_V^2 (1 - c_H^2 \xi^2) = m_W^2 M_\pm^2, \\ \tan 2\theta_C &= \frac{2c_H \xi \hat{m}_W \hat{m}_V}{\hat{m}_V^2 - \hat{m}_W^2}. \end{aligned} \quad (1.9)$$

By checking Eq. (1.6) and Eq. (1.8), the charged and neutral mass matrices are connected by custodial symmetry, which can be shown in full generality to imply

$$\mathcal{M}_C^2 = \begin{pmatrix} \cos \theta_W & 0 \\ 0 & 1 \end{pmatrix} \mathcal{M}_N^2 \begin{pmatrix} \cos \theta_W & 0 \\ 0 & 1 \end{pmatrix}. \quad (1.10)$$

By taking the determinant of the above equation, or equivalently by comparing the charged and neutral determinants in Eq. (1.7) and Eq. (1.9), we obtain a generalized custodial relation among the physical masses

$$m_W^2 M_{\pm}^2 = \cos^2 \theta_W m_Z^2 M_0^2. \quad (1.11)$$

From the simple formula above, we can start to identify the physically reasonable region of the parameter space in this model. We aim at describing new vectors with masses at or above the TeV scale, but we also want the SM masses $m_{W,Z} \sim 100$ GeV to be reproduced. Therefore we require a hierarchy in the mass relation of SM Z and W bosons versus the new vectors.

$$\frac{\hat{m}_{W,Z}}{\hat{m}_V} \sim \frac{m_{W,Z}}{M_{\pm,0}} \leq 10^{-1} \ll 1 \quad (1.12)$$

In the limit of Eq. (1.12) we obtain simple approximation for m_W and m_Z

$$\begin{aligned} m_Z^2 &= \hat{m}_Z^2 (1 - c_H^2 \xi^2) (1 + \mathcal{O}(\hat{m}_Z^2 / \hat{m}_V^2)), \\ m_W^2 &= \hat{m}_W^2 (1 - c_H^2 \xi^2) (1 + \mathcal{O}(\hat{m}_W^2 / \hat{m}_V^2)). \end{aligned} \quad (1.13)$$

The parameter ξ can be either very small or of order unity. Both cases are realized in explicit models. While $\xi \ll 1$ is the most common situation, $\xi \sim 1$ only occurs in strongly coupled scenarios at very large g_V . In these approximations, SM tree-level experimental observation can be reproduced to percent accuracy.

Since $\hat{m}_W = \cos \theta_W \hat{m}_Z$, the W - Z mass ratio is thus given by

$$\frac{m_W^2}{m_Z^2} \simeq \cos^2 \theta_W . \quad (1.14)$$

Eq. (1.14) has one important implication on the masses of the new vectors. When combined with the custodial relation Eq. (1.11), it tells us that the charged and neutral V s are practically degenerate

$$M_{\pm}^2 = M_0^2(1 + \mathcal{O}(\%)) , \quad (1.15)$$

⁵⁶ In the following, when working at the leading order in the limit Eq. (1.12), we can
⁵⁷ ignore the mass splitting and denote the mass of the charged and the neutral states
⁵⁸ collectively as M_V . It is easy to check that in that limit $M_V = \hat{m}_V$.

⁵⁹ Decay Widths

Because of the hierarchy in the mass matrices, the mixing angles are naturally small. By looking at Eqs. (1.7), (1.9) and (1.12) we can estimate

$$\theta_{N,C} \simeq c_H \xi \frac{\hat{m}_{W,Z}}{\hat{m}_V} \leq 10^{-1} , \quad (1.16)$$

and after rotating to the mass basis, the coupling of the neutral and charged resonances to left- and right-handed fermion chiralities can be written in a compact form for each fermion species $F = \{l, q, 3\}$.

$$\begin{cases} g_L^N = \frac{g^2}{g_V} \frac{c_F}{2} \cos \theta_C + (g_L^Z)_{SM} \sin \theta_N \simeq \frac{g^2}{g_V} \frac{c_F}{2} , \\ g_R^N = (g_R^Z)_{SM} \sin \theta_N \simeq 0 \\ g_L^C = \frac{g^2}{g_V} \frac{c_F}{2} \cos \theta_C + (g_L^W)_{SM} \sin \theta_C \simeq \frac{g^2}{g_V} \frac{c_F}{2} , \\ g_R^C = 0 \end{cases} \quad (1.17)$$

In the above equation $(g_{L,R}^{W,Z})_{SM}$ denote the ordinary SM W and Z couplings (with the normalization given by $g_L^W = g/\sqrt{2}$).

Given that the rotation angles are small, the couplings further simplify, as also shown in the equation. We could see that V interact mainly with left-handed chiralities and that all the couplings for each fermion species are controlled by the parameter combination g^2/g_{VC_F} . This gives tight correlations among different channels

$$\Gamma_{V_\pm \rightarrow f\bar{f}'} \simeq 2\Gamma_{V_0 \rightarrow f\bar{f}'} \simeq N_C[f] \left(\frac{g^2 c_F}{g_V}\right)^2 \frac{M_V}{48\pi}, \quad (1.18)$$

where $N_C[f]$ is the number of colors (3 for the di-quark and 1 for the dilepton decays). The parameters $c_F = \{c_l, c_q, c_3\}$ control the relative BRs to leptons, light quarks and the third family.

In the case of di-boson decay width

$$\begin{aligned} \Gamma_{V_0 \rightarrow W_L^+ W_L^-} &\simeq \Gamma_{V_\pm \rightarrow W_L^\pm Z_L} \simeq \frac{g_V^2 c_H^2 M_V}{192\pi} \frac{(1 + c_H c_{VVV} \xi^2)^2}{(1 - c_H^2 \xi^2)^2} = \frac{g_V^2 c_H^2 M_V}{192\pi} [1 + \mathcal{O}(\xi^2)], \\ \Gamma_{V_0 \rightarrow Z_L h} &\simeq \Gamma_{V_\pm \rightarrow W_L^\pm h} \simeq \frac{g_V^2 c_H^2 M_V}{192\pi} \frac{(1 - 4c_{VVHH} \xi^2)^2}{1 - c_H^2 \xi^2} = \frac{g_V^2 c_H^2 M_V}{192\pi} [1 + \mathcal{O}(\xi^2)]. \end{aligned} \quad (1.19)$$

⁶⁰ Note that Eq. (1.19) is derived in the Equivalent Gauge [16] because the decay to transverse SM vectors is highly suppressed while to the longitudinal parts grows with the energy of the process, therefore the Unitary Gauge which is used in the original Lagrangian is instead useful. The channels that are not shown in the above equations are either forbidden or suppressed like the decays to transverse polarizations.

⁶⁵ From this section, a very simple picture emerges. At small ξ , all the decay widths are fixed with a given resonance mass M_V and the couplings $\{g^2 c_F/g_V, g_{VC_H}\}$ which control the BRs in all relevant channels. Parameters c_{VVV} , c_{VVHH} and c_{VWW} are basically irrelevant. Thus, the basic phenomenology of this model is well described by a good approximation.

⁷⁰ 1.2.3 Explicit Models

Now the general picture is clear, we can get exact values of the widths and BRs from explicit models. Consider two benchmark models, A and B, which correspond to two explicit models describing the heavy vectors in Refs. [17] and [12] respectively. All the c parameters are fixed to specific values in these models and the only free parameters are the resonance mass M_V and coupling g_V . Moreover, model A is inspired by weakly coupled extensions of the SM gauge group while model B is by strongly coupled scenarios of EWSB, *i.e.* Composite Higgs models, we will consider them in different regions of g_V , relatively small $g_V \leq 3$ and relatively large $g_V \geq 3$.

Figure 1-1 shows the BRs as functions of the mass in model A and B. As expected from the previous discussion and according to Refs. [17], model A predicts

$$c_H = -g^2/g_V^2, c_F \simeq 1, \\ |g_V c_H| \simeq g^2 c_F / g_V \simeq g^2 / g_V. \quad (1.20)$$

Therefore Eq. (1.18) and (1.19) can be determined in the following form for V_0 in model A ($g_V = 1$),

$$\Gamma_{V_0 \rightarrow f\bar{f}'} \simeq N_c[f] \frac{g^4 M_V}{96\pi} \\ \Gamma_{V_0 \rightarrow W^+W^-} \simeq \Gamma_{V_0 \rightarrow Zh} \simeq \frac{g^4 M_V}{192\pi}. \quad (1.21)$$

One can easily check either from the plot or the equation, a factor of two difference comparing the BRs between fermions and bosons. Due to the color factor, leptons and quarks also have a difference by a factor of three. Since the c_F term is universal both in A and B. The total width in model A decreases with increasing g_V because of the overall suppression (g^2/g_V) in Eq. (1.20).

On the contrary, in model B the c_H term is unsuppressed

$$c_H \simeq c_F \simeq 1 , \\ g_V c_H \simeq -g_V , g^2 c_{c_F} / g_{g_V} \simeq g^2 / g_V . \quad (1.22)$$

Thus the determinate V_0 decay widths for model B ($g_V = 3$) are

$$\Gamma_{V_0 \rightarrow f\bar{f}'} \simeq N_c[f] \frac{g^4 M_V}{342\pi} \\ \Gamma_{V_0 \rightarrow W^+W^-} \simeq \Gamma_{V_0 \rightarrow Zh} \simeq \frac{3M_V}{64\pi} . \quad (1.23)$$

⁷¹ For model B _{$g_V=3$} the dominant BRs are into di-bosons and the fermionic decays are
⁷² extremely suppressed. Moreover, the total width increases with increasing g_V since it
⁷³ is dominated by the di-boson width which grows with g_V as expected from Eq. (1.22).
⁷⁴ This model B is particularly interesting for the present search, since it predicts signal
⁷⁵ cross sections of the order of fb [15] [18] [Fig. 1-2], branching ratios to vector bosons
⁷⁶ close to unity, and thus being accessible at the LHC. In the latter chapters, the mass
⁷⁷ eigenstate of the neutral heavy vector boson in model B scenario refers to the Z'
⁷⁸ particle, which is the search target of this thesis.

⁷⁹

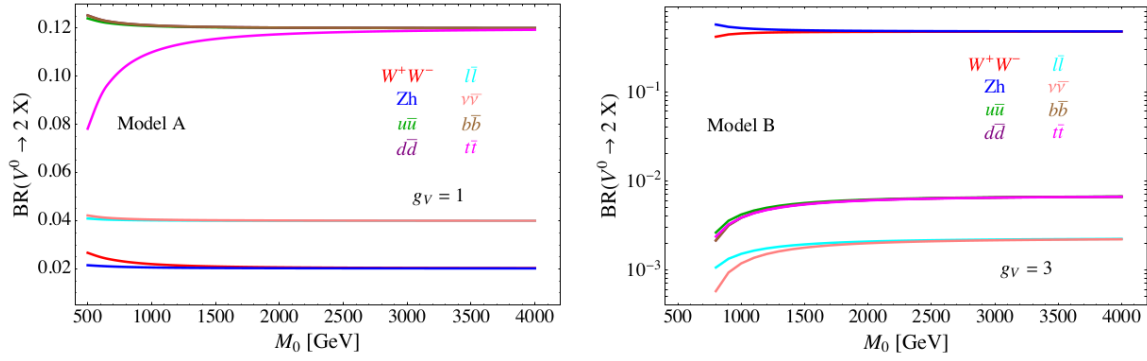


Figure 1-1: Branching ratios as a function of the resonance mass for the HVT benchmark model A(left) and model B(right).

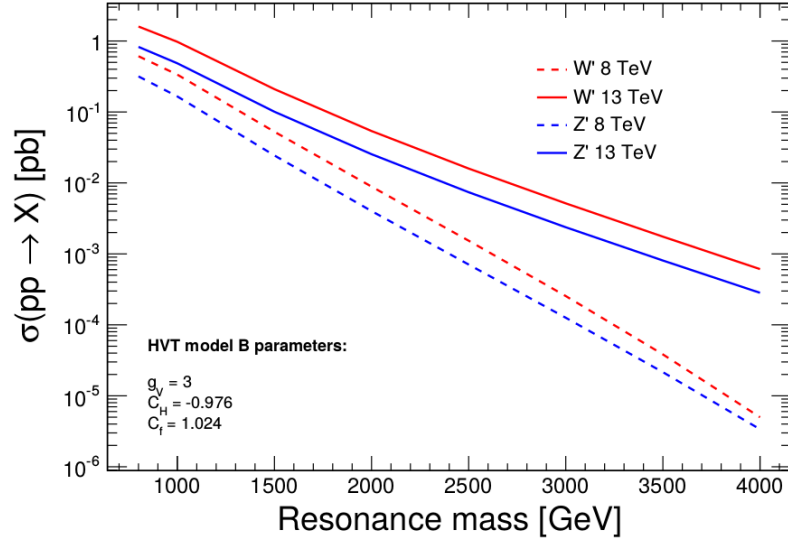


Figure 1-2: Theoretical production cross-section as a function of new resonance particles for HVT model B benchmark. Dash lines are 8 TeV predictions while solid lines are 13 TeV predictions.

80 **Chapter 2**

81 **CMS detector and LHC**

82 This thesis is based on the data collected by the Compact Muon Solenid (CMS)
83 detector at the Large Hadron Collider (LHC). CMS is one of the two largest detectors
84 built at the LHC. This chapter will briefly introduce the LHC and the CMS detector.

85 **2.1 Large Hadron Collider**

86 The LHC is the world’s most powerful hadron collider and the largest experimental
87 facility ever. It was built by the European Organization for Nuclear Research (CERN)
88 between 1998 and 2008 in collaboration with over 10,000 scientists and engineers from
89 over 100 countries, as well as hundreds of universities and laboratories. It lies in a
90 tunnel 27 km in circumference, as deep as 175 m beneath the France–Switzerland
91 border near Geneva. The designed maximum collision energy and highest luminosity
92 of the LHC are 14 TeV and $10^{-34}\text{cm}^{-2}\text{s}^{-1}$, respectively.

93 Other accelerators that had been originally built at CERN for previous experi-
94 ments serve as an injection chain for the LHC now (shown in Fig. 2-2). The proton
95 beam starts from LINAC, a small linear accelerator, where the energy of protons first
96 reaches at 50 MeV. The proton beam then passes through a booster and goes to the
97 PS, where it is accelerated up to 25 GeV. After that, it reaches 450 GeV in the SPS.
98 The beam is finally injected in the LHC ring from the SPS, and it had been acceler-
99 ated up to 4 TeV in 2012. In early 2015, the proton beam had been acceleated to

100 6.5 TeV, a value near its designed energy, before undergoing collision.

101 There are four collision points at the LHC, corresponding to four main experiments, CMS, ATLAS, LHCb and ALICE. The ALICE experiment is optimized to
102 study heavy-ion (Pb-Pb nuclei) collisions and focusing on the physics of strongly
103 interacting matter at extreme energy densities. LHCb is a specialized b-physics ex-
104 periment, measuring the parameters of CP violation in the interactions of b-hadrons.
105 Such studies can help to explain the matter-antimatter asymmetry of the universe.
106 Last, CMS and ATLAS are two general purpose detectors. The aims of these two
107 experiments are investigating a wide range of physics, including the search for the
108 beyond standard model particles, extra dimensions, and dark matter.



Figure 2-1: Overview of the LHC and relative location of the detectors.

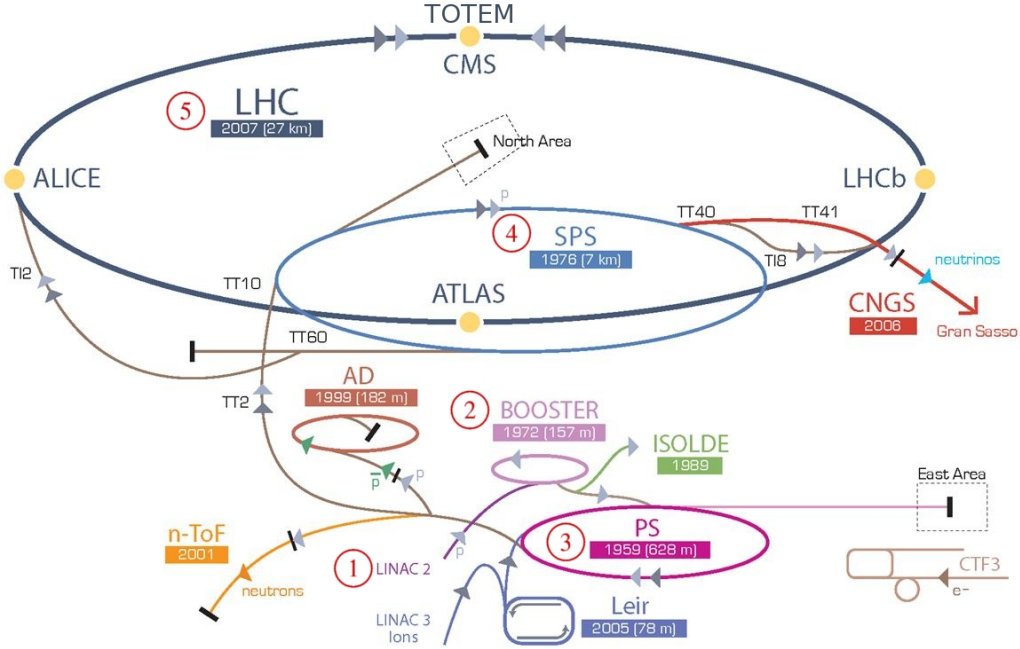


Figure 2-2: CERN accelerator complex.

2.2 Compact Muon Solenoid

The Compact Muon Solenoid (CMS) is designed to cope very high rate of interactions expected to take place at the high LHC luminosity. It has the typical structure of detectors at hadron colliders: a central region (*barrel*) enclosed by two disks (*endcaps*). The structure of CMS can be seen in Fig. 2-3.

Solenoid and Sub-detectors

CMS features a powerful superconducting coil, generating a solenoidal magnetic field around 3.8 Tesla in a large volume which hosts different sub-detectors. The magnetic field lines close through steel yoke in the outer region. The distinct sub-detectors are designed in order to obtain the highest possible resolution and the largest acceptance for every kind of particles.

The innermost layer is a silicon-based tracker. Surrounding it is a scintillating crystal electromagnetic calorimeter (ECAL), which is itself surrounded with a sampling calorimeter for hadrons (HCAL). The tracker and the calorimeters are compact

¹²⁴ enough to fit inside the CMS Solenoid. Outside the magnet are the large muon
¹²⁵ chambers.

CMS Detector

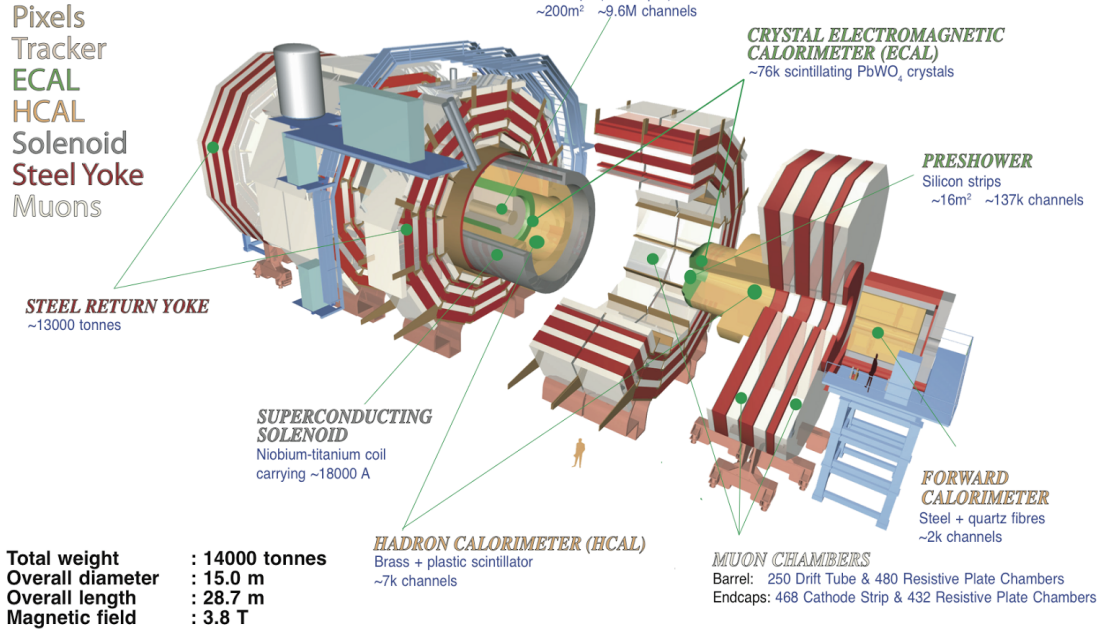


Figure 2-3: Structure overview of the CMS detector.

¹²⁶ Coordinate System

¹²⁷ The CMS coordinate system is oriented such that the x -axis points to the center of
¹²⁸ the LHC ring, the y -axis points vertically upward and the z -axis is in the direction
¹²⁹ of the beam. The azimuthal angle ϕ is measured from the x -axis in the $x - y$ plane
¹³⁰ and the radial coordinate in this plane is denoted by r . The polar angle θ is defined
¹³¹ in the $r - z$ plane, while the pseudo-rapidity $\eta = -\ln \tan(\theta/2)$. The momentum
¹³² component transverse to the beam direction, denoted by p_T , is computed from the x -
¹³³ and y -components, and the transverse energy is defined as $E_T = E \sin \theta$.

¹³⁴ **2.2.1 Tracker**

¹³⁵ Tracker is the most inner part of CMS that records the productions of collisions in the
¹³⁶ first place. It traces the charged particles' trajectories. Physicists can reconstruct the
¹³⁷ vertices of the interaction and the momentum of charged particles by linking tracks
¹³⁸ to the collider's pipe and measuring the curves of particles under magnetic field.

¹³⁹ The tracking system is composed of two kinds of detector, the pixel detector and
¹⁴⁰ silicon strip detector. The pixel detector is built from three barrel layers at $r = 44$,
73, 102 mm, and two endcap disks on each side at $z = \pm 345, \pm 465$ mm.

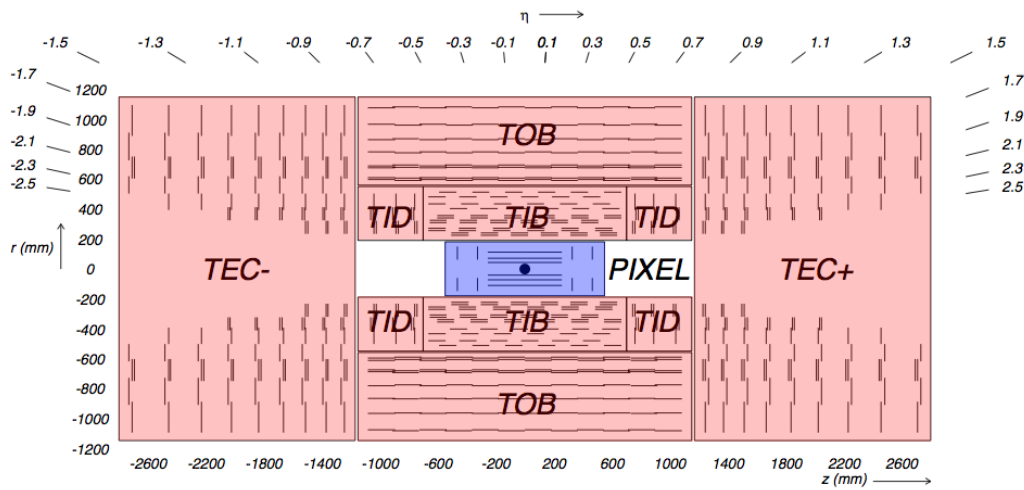


Figure 2-4: Schematic layout of tracker.

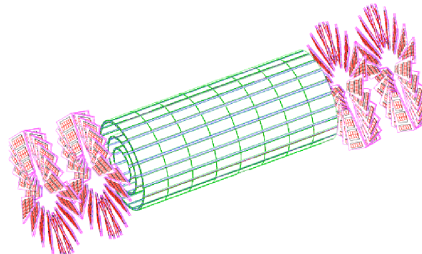


Figure 2-5: The pixel detector inside tracker.

¹⁴¹
¹⁴² The pixel detector consists of 1440 segmented silicon sensor modules with total 66 mil-
¹⁴³ lion readout channels. Charge carriers are distributed over several pixels. The analog

144 pulse height information can be used to calculate the center of certain charge distribution
145 which could improve the hit information. The spatial resolution is measured
146 to be about $10 \mu\text{m}$ for the $r - \phi$ plane or about $20 \mu\text{m}$ for z direction measurement.

147 Outside the pixel detector, there comes the silicon strip detector. The barrel
148 region of silicon strip detector is divided into two parts, the Tracker Inner Barrel
149 (TIB) and the Tracker Outer Barrel (TOB). The former is composed of four layers
150 of silicon sensors with a thickness of $320 \mu\text{m}$ and of strip pitches varying from 80
151 to $120 \mu\text{m}$. The TOB is made of six layers. In this kind of sub-detector, thicker
152 silicon sensors ($500 \mu\text{m}$) are employed, while the strip pitch varies from 120 to 180
153 μm . The endcap region ($|\eta| > 1.6$) is covered by the Tracker Inner Disks (TID)
154 and the Tracker End Cap (TEC). The entire silicon strip detector is comprised of
155 15200 high-sensitivity modules consisting of detecting unit, supporting structure and
156 readout electronic system.

157 2.2.2 ECAL

158 The Electromagnetic Calorimeter (ECAL) measures the energy of photons, electrons
159 and positrons. It it is placed just outside the tracker, but still inside the solenoid.
160 ECAL is made of 74848 lead-tungstate (PbWO_4) crystals. This material is charac-
161 terized by a high density (8.28 g/cm^3), which gives the crystals a very compact form
162 and makes them particularly suitable to be placed inside the magnetic coil. Another
163 reason, this material has also a fast temporal response ($\sim 10 \text{ ns}$) and its radiation
164 length (X_0) of 0.89 cm give ECAL the possibility to fully contain the expansion of
165 the electromagnetic shower.

166 The arrangement of ECAL is shown in Fig. (2-6). The barrel crystals have a front
167 face area of $2.2 \times 2.2 \text{ cm}^2$ and a length of 23 cm. They are positioned at $r = 1.29$
168 m in pseudo-rapidity region $0 < |\eta| < 1.479$. The crystals in the endcaps have a
169 $2.47 \times 2.47 \text{ cm}^2$ front face, a 22 cm length and they are positioned at $z = 3.17 \text{ m}$ in
170 $1.479 < |\eta| < 3.0$. A Preshower detector is placed in front of the endcaps crystals.
171 The active elements of Preshower are two planes of silicon strips with a pitch of 1.9
172 mm, which lie behind disks of lead absorber at depths of $2X_0$ and $3X_0$. It allows the

₁₇₃ rejection of photon pairs from π^0 decays and improves the estimation of the direction
₁₇₄ of photons, to enhance the measurement of the two-photon invariant mass.

The energy resolution of the ECAL is given by three different contributions [19] (E in GeV),

$$\frac{\sigma_E}{E} = \frac{2.8\%}{\sqrt{E}} \oplus \frac{12\%}{E} \oplus 0.3\% \quad (2.1)$$

₁₇₅ where the first term is statistical in nature, it also contains fluctuation in showering
₁₇₆ and in the amplification through photodiodes, the second one considers electronic
₁₇₇ noise and pile-up, the last term is mainly due to the calibration.

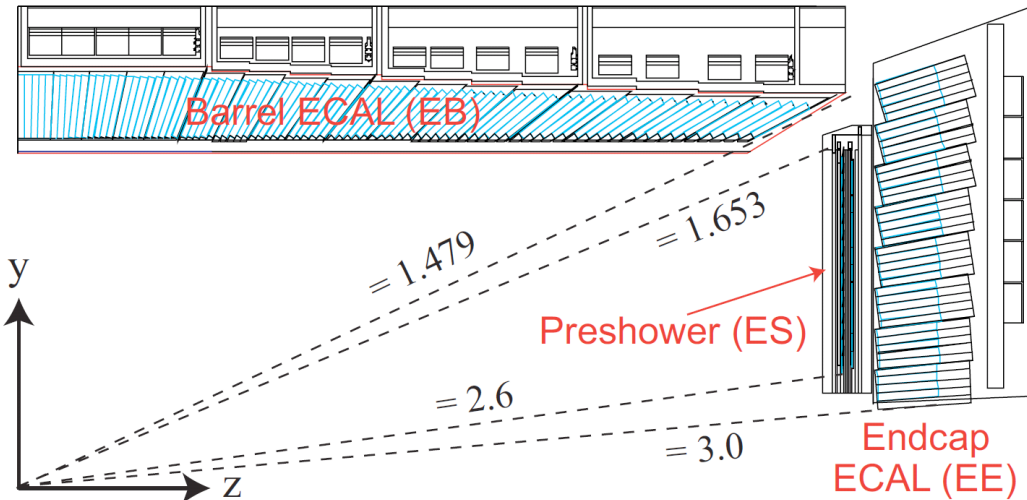


Figure 2-6: Schematic layout of the CMS ECAL.

₁₇₈ 2.2.3 HCAL

₁₇₉ The hadron calorimeter (HCAL) is placed mainly between ECAL and the magnet
₁₈₀ coil. It measures the energy of hadrons and mesons. Additionally it provides indirect
₁₈₁ measurement of the presence of non-interacting, uncharged particles such as neutrinos.
₁₈₂ The design is strongly influenced by these aims, hence an important requirement is the
₁₈₃ high hermeticity (the ability to capture every particle emerging from the collisions).
₁₈₄ This means the detector must cover the biggest possible portion of the solid angle.

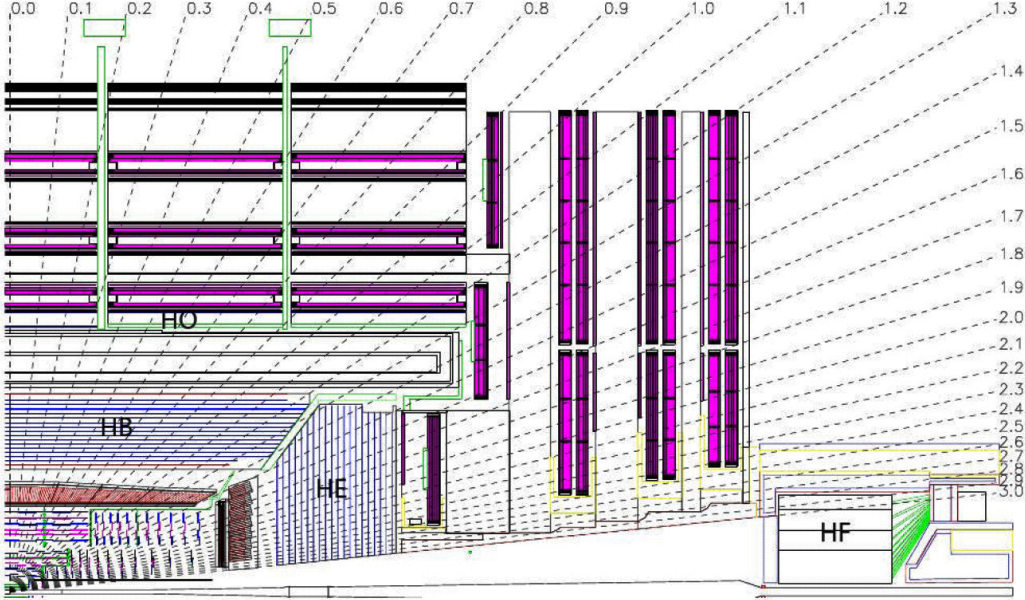


Figure 2-7: Longitudinal view of one quarter of CMS and the location of HB (hadron barrel calorimeter), HE (hadron endcap calorimeter), HF (hadron forward calorimeter) and HO (hadron outer calorimeter)

185 For this reason, a hadron forward calorimeter is required, which is placed outside
 186 the magnet return yokes, with a total coverage of $3 < |\eta| < 5.31$ at 11 m from the
 187 interaction point. Moreover, an outer hadronic calorimeter is placed in the first muon
 188 absorber layer in order to enhance the containment of high energy jets in the central
 189 region of the detector.

190 HCAL is a sampling calorimeter, whose active elements are plastic scintillators
 191 interleaved with brass absorber plates and read out by wavelength shifting fibers.
 192 Brass has been chosen as absorber material for its short interaction length and because
 193 it is non-magnetic. The thickness of the absorber layers is between 60 mm in the barrel
 194 and 80 mm in the endcaps. The barrel has 5.46 interaction lengths at $\eta = 0$ and 10.82
 195 at $\eta = 1.3$, while the endcaps have an average of 11 interaction lengths [20].

The HCAL energy resolution (E in GeV and measured by pion) [21] is

$$\frac{\sigma_E}{E} \simeq \frac{a}{\sqrt{E}} \oplus 5\% \quad (2.2)$$

196 where $a \simeq 65\%$ in the barrel, $a \simeq 85\%$ in the endcaps and $a \simeq 100\%$ in the HF.

2.2.4 Muon Chamber

The efficient detection of muons has primary importance, as muons represent a clear signature for a large number of processes. Muons can penetrate several meters of iron without interacting. Unlike most particles, they are not stopped by any of calorimeters in CMS. Therefore, chambers to detect muons are placed at the very edge of the experiment where they are the only particles likely to register a signal.

The muon system fulfills three purposes, muon identification, momentum measurement and triggering. Three different types of gaseous detectors are used for CMS muon system depending on the requirements.

Drift Tube

The drift tube (DT) system measures muon positions in the barrel part of the detector. Each DT chamber, on average $2\text{ m} \times 2.5\text{ m}$ in size, consists of 12 aluminium layers, arranged in three groups of four segmentations, each with up to 60 4-cm-wide tubes that contain a stretched wire within each gas volume. The middle group measures the coordinate along the direction parallel to the beam and the two outside groups measure the perpendicular coordinate.

Cathod Strip Chamber

In the two endcaps, where the muon flux and the residual inhomogeneous magnetic field are higher, cathode strip chambers (CSC) are used. CSC is composed of anode wires and cathod strips in the gas volume. The chambers are arranged in 4 disks perpendicular to the beam, and in concentric rings (3 rings in the innermost station, 2 in the others) in each of the endcaps.

Resistive Plate Chambers

Resistive plate chambers (RPC) are fast gaseous detectors that provide a muon trigger system parallel with DTs and CSCs. Each RPC consists of two parallel plates, a

222 positively charged anode and a negatively charged cathode, both made of a very high
223 resistivity plastic material and separated by a gas volume.

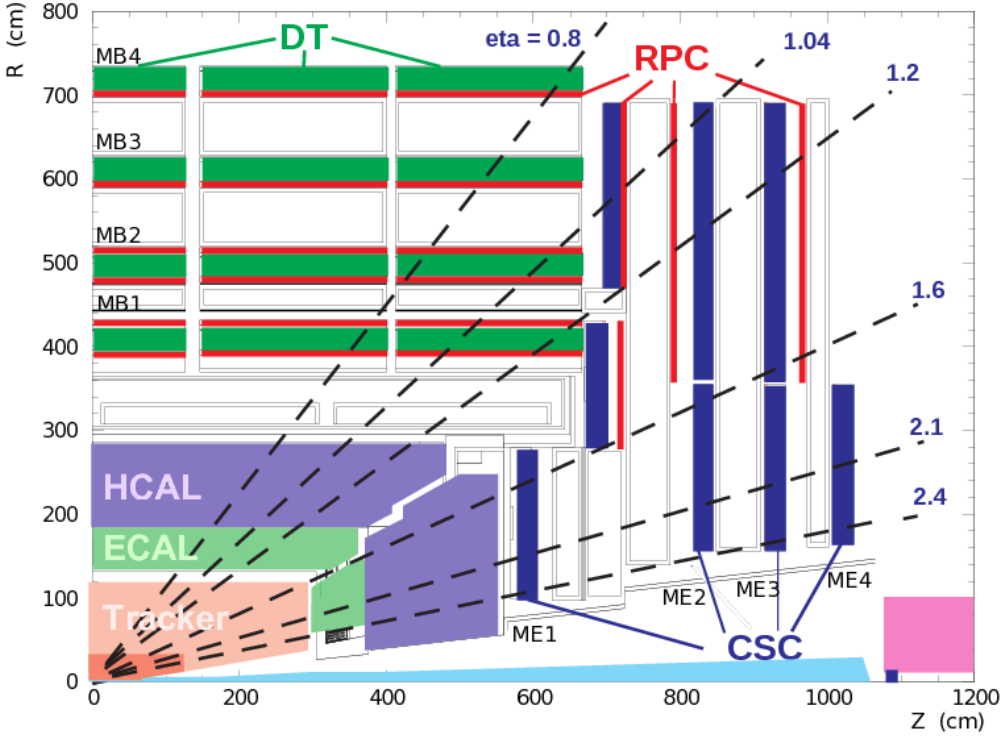


Figure 2-8: Slice view of one quarter of muon chamber system.

224 2.2.5 Trigger System

225 To have a good chance of producing rare particles, a very large number of collisions
226 is required (LHC proton bunches collide every 25 ns). Most collision events in the
227 detector are soft and do not produce interesting events. The amount of data from
228 each crossing is approximately 1 megabytes, which at the 40 MHz crossing rate would
229 result in 40 terabytes of data a second, an amount that the experiment cannot store.
230 The task of the trigger system is to reduce the storage rate while keeping a high
231 efficiency on the potentially interesting events. In CMS the input rate is reduced in
232 two steps, Level-1 Trigger (L1T) and High-Level Trigger (HLT).

233 **Level-1 Trigger**

234 After the Level-1 Trigger selection, the event recording frequency is decreased to
235 100kHz [22], which is much smaller than the collision rate. The L1T objects are
236 particles (such as photons, muons and electrons), jet candidates, global transverse
237 energy and missing transverse energy. Level-1 Trigger just choose the event with E_T
238 and P_T higher than the thresholds.

239 **High Level Trigger**

240 High Level Trigger is behind the readout buffers after Level-1 Trigger. It reduces
241 the data output rate to 100Hz by using all the information from CMS including the
242 sub-detectors. The reconstruction algorithms are the same as the off-line analysis.
243 However, the triggering procedure doesn't need maximal precision, therefore these
244 algorithms are modified to be faster even with lower resolution.

245

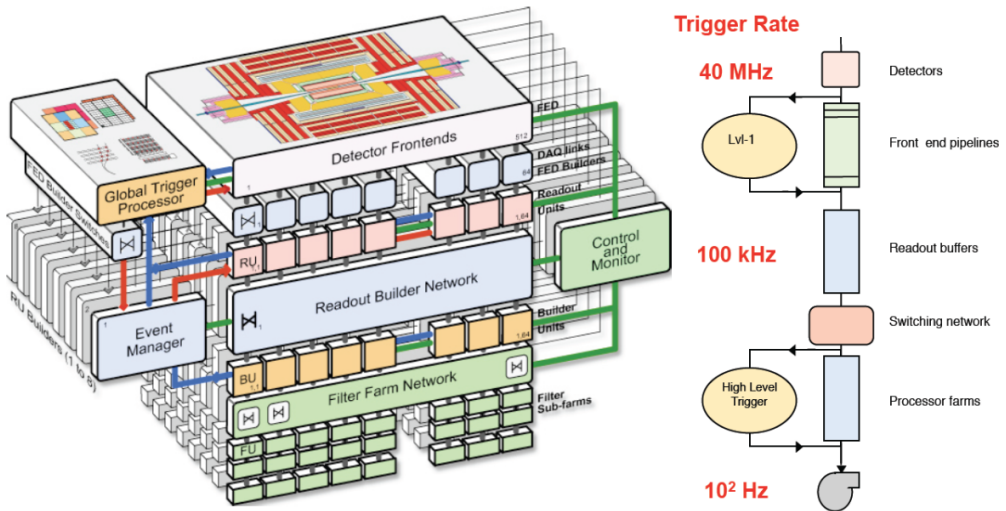


Figure 2-9: CMS triggering and data acquisition architecture.

246 **Chapter 3**

247 **Analysis Procedures**

248 In this chapter, the analysis procedures of the search for Z' decaying into $Z h$ in $llbb$
249 final state are reported. The data sets and Monte Carlo (MC) samples we used in this
250 analysis will be indicated. Physics objects reconstruction and event selections are also
251 introduced. Moreover, background yields and the effects of systematic uncertainties
252 will be demonstrated in the end of this chapter.

253 **3.1 Monte Carlo Samples and Data sets**

254 **3.1.1 Signal MC**

255 As introduced in section 1.2.3, the signal hypothesis is HVT model B benchmark.
256 The heavy resonance (Z') is tested using a wide set of masses from 800 GeV to
257 2000 GeV, one masspoint every 100 GeV (Table 3.1). The signal is simulated by
258 MadGraph5_aMC@NLO [23] in LO mode, as a narrow spin-1 neutral resonance and
259 is forced to decay in the $Z' \rightarrow Z h \rightarrow llqq$ channel. Showering and hadronization are
260 performed with PYTHIA6 [24].

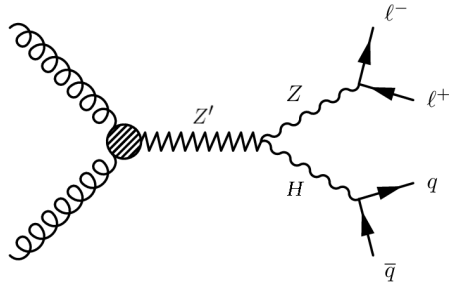


Figure 3-1: Feynman diagram for $Z' \rightarrow Zh \rightarrow 2l2q$.

Sample	Number of Processed Events	$\sigma_{LO}(\text{pb})$
ZPrime_ZH_lljj_M800-MADGRAPH	10710	0.00685367
ZPrime_ZH_lljj_M900-MADGRAPH	10209	0.00485861
ZPrime_ZH_lljj_M1000-MADGRAPH	19997	0.003263
ZPrime_ZH_lljj_M1100-MADGRAPH	9370	0.00217483
ZPrime_ZH_lljj_M1200-MADGRAPH	10710	0.00145484
ZPrime_ZH_lljj_M1300-MADGRAPH	9369	0.000979745
ZPrime_ZH_lljj_M1400-MADGRAPH	10497	0.000664783
ZPrime_ZH_lljj_M1500-MADGRAPH	19999	0.000454339
ZPrime_ZH_lljj_M1600-MADGRAPH	8950	0.000312541
ZPrime_ZH_lljj_M1700-MADGRAPH	9369	0.000216282
ZPrime_ZH_lljj_M1800-MADGRAPH	10708	0.000150398
ZPrime_ZH_lljj_M1900-MADGRAPH	10498	0.000105039
ZPrime_ZH_lljj_M2000-MADGRAPH	19999	7.36377e-05

Table 3.1: Signal samples used in the analysis.

261 **3.1.2 Background MC**

262 Since we are looking for new resonances decaying in semi-leptonic final state, the
263 background samples of this analysis are originated by all SM events with two leptons
264 and at least one jet as final state. The dominant background contribution is the
265 production of Z boson with jets. This Z+jets sample is produced by MADGRAPH.
266 In the matrix element level, the Z boson is forced decaying into two leptons, and
267 further this sample is divided into two samples depending on the Z p_T , higher than
268 100 GeV or between 70 and 100 GeV. The contribution of events with Z p_T less than
269 70 GeV is negligible due to further cut on the objects p_T in the selection criteria.

270 The second dominant source of background is $t\bar{t}$ production. Both of the two top
271 quarks decay into all leptonic final state (top decays into a W boson and a b quark
272 first) which gives two leptons, neutrinos and two b-jets. This sample is generated by
273 POWHEG [25].

274 Other sources of background considered are SM di-boson productions (WW, WZ
275 and ZZ) generated by PYTHIA6. All the background samples are required to pass
276 phase-space cuts, $p_T^l > 60$ GeV and $60 < M_{ll} < 120$ GeV. Related statistics are reported
277 in Table 3.2.

Sample	Number of Processed Events	$\sigma_{NLO}(\text{pb})$
DYJetsToLL_PtZ-70To100	11764538	63.5
DYJetsToLL_PtZ-100	12511326	39.4
TTTo2L2Nu2B	10783509	25.8
WW	7759752	$56.0 \pm 2.3 (\pm 0.3)$
WZ	9910267	22.4
ZZ	9769891	$7.6 \pm 0.3 (\pm 0.3)$

Table 3.2: Background samples used in the analysis.

278 **3.1.3 Data Samples**

279 In this analysis, the full CMS data collected in 2012 is used, corresponding to the
280 integrated luminosity of 19.7 fb^{-1} at center-of-mass energy $\sqrt{s} = 8$ TeV. For each
281 lepton channel, there are four datasets. All datasets are collected with a double

muon or a double electron trigger, as explained in detail in the next section. The trigger algorithm employed for the electron samples doesn't use any information from the tracker but only the energy deposite in the ECAL. This expedient is implemented in order to avoid any possible inefficiencies due to the presence of two tracks very close to each other when the Z is highly boosted and its decay products are very collimated. Such a trigger is contained in the Photon/DoublePhotonHighPt dataset.
 The full dataset names are listed in Table 3.3.

AOD Sample	Luminosity (pb^{-1})
DoubleMu/Run2012A-22Jan2013-v1	876.225
DoubleMuParked/Run2012B-22Jan2013-v1	4409
DoubleMuParked/Run2012C-22Jan2013-v1	7017
DoubleMuParked/Run2012D-22Jan2013-v1	7369
Photon/Run2012A-22Jan2013-v1	876.225
DoublePhotonHighPt/Run2012B-22Jan2013-v1	4412
DoublePhotonHighPt/Run2012C-22Jan2013-v1	7055
DoublePhotonHighPt/Run2012D-22Jan2013-v1	7369

Table 3.3: Data sets used in this analysis.

3.2 Trigger

Since the final state contains two same flavour leptons and at least one jet, we perform this analysis on the DoubleMu and Photon/DoublePhotonHighPt datasets. The first dataset is triggered by two muons, the second one is triggered by two eletrons. These triggers are:

- HLT_Mu22_TkMu8* (for DoubleMu datasets)
- HLT_DoubleEle33_*(for Photon/DoublePhontonHighPt datasets)

The muon trigger has a double p_T threshold, requires leading muon p_T greater than 22 GeV and sub-leading muon p_T greater than 8 GeV. Differently, the double electron trigger requires a higher threshold of 33 GeV to electrons. The trigger efficiencies are close to 1 in both cases.

300 **3.3 Physics Objects**

301 **3.3.1 Muon**

302 **Reconstruction**

303 The muon reconstruction algorithm at CMS takes advantage of the redundancy of
304 detection methods. Muon tracks are first reconstructed independently in the inner
305 tracker (tracker track) and in the muon system (standalone track). Based on these
306 objects, two reconstruction approaches are used [26]:

307 • *Globol Muon* (outside-in): Starting from a standalone track, this algorithm
308 finds a best tracker track to match the standalone track. Then, the fit of the
309 track is repeated using the hits both in the tracker and in the muon system [27].
310 The resulting object is called a *Global Muon*. At large transverse momentum
311 ($p_t > 200$ GeV), the global muon fit can improve the momentum resolution
312 compared to the tracker only fit.

313 • *Tracker Muon* (inside-out): A tracker muon is reconstructed by an opposite
314 direction from a global muon. In this approach, all tracker tracks with $p_T >$
315 0.5 GeV and the total momentum $p > 2.5$ GeV are considered as possible
316 muon candidates. The extrapolation to the muon system takes into account the
317 magnetic field, average expected energy losses, and multiple scattering in the
318 detector material. If at least one muon segment matches the extrapolated track,
319 the corresponding track track qualifies as a *Tracker Muon*. This algorithm is
320 useful for low- p_T muons that are not fully penetrate the muon system, and
321 therefore only register a few hits

322 If no match is found when extrapolating outside-in, the standalone track is stored
323 as a *Stanalone Muon*. This happens only for less than 1% of the muons produced in
324 a collison, and the reconstruction efficiency is about 99% for the muon which carries
325 enough high momentum within detector coverage [26].

326 **Identification**

327 We use both tracker muons and global muons in this analysis. To identify muons
328 from the signal, the muons must pass one of these two off-line selections, high- p_T
329 muon ID or tracker-based muon ID [28]. The requirements are listed as follows:

330

331 High- p_T muon ID

- 332 • Muon identified as a *Global Muon*.
333 • Number of muon hits in the global track > 0 .
334 • Number of matched muon stations > 1 .
335 • Number of pixel hits > 0 .
336 • Number of tracker layer with hits > 8 .
337 • Transverse impact parameter $d_{xy} < 0.2$ cm.
338 • Longitudinal impact parameter $d_z < 0.5$ cm.
339 • Relative error on the track transverse momentum $\sigma_{p_T}/p_T < 0.3$.

340

341 In the tracker-based muon ID, the muon has to be identified as a *Tracker Muon*,
342 and the requirement of muon hits in the global track is removed. Other requirements
343 are the same.

344 An additional useful variable for lepton identification is the isolation. It is defined
345 as the scalar sum of the p_T of the reconstructed objects within a cone (typical size
346 is $\Delta R = 0.3$) space around the lepton track but excluding the p_T of the lepton
347 itself. Moreover, the relative isolation is defined as isolation divided by the lepton
348 p_T ($I_{rel} = Iso/p_T^{lept}$). The relative isolation is more frequently used in the modern
349 analysis.

350 In this analysis, a modified isolation criteria is used. The two muons originated
351 from boosted Z decay are close to each other, and consequently the presence of another

352 muon in the isolation cone could break the function of this variable. To solve this
353 problem, we exclude the energy contribution of muons inside the cone.

$$I_{rel}^{mod} = \frac{\sum p_T^{CH} + \max(0.0, \sum_{lep} E_T^{NH} + \sum E_T^\gamma - 0.5 \times \sum p_T^{PU})}{p_T} \quad (3.1)$$

354 In the above equation, p_T^{CH} denotes the charged hadron transverse momentum
355 inside the cone. Similarly, E_T^{NH} and E_T^γ stand for neutral hadron and photon trans-
356 verse energy respectively. The last term in the nominator, $\sum p_T^{PU}$ is defined as sum
357 of transverse momentum of the charged particles in the cone but with particles not
358 originating from the primary vertex (for pile-up corrections). Finally, the modified
359 requirement is $I_{rel}^{mod} < 0.1$.

360

Variable	High- p_T	Tracker-based
Muon type	Global muon	Tracker muon
Muon hits in global track	≥ 1	-
Muon stations matched	≥ 2	≥ 2
d_{xy}	< 0.2 cm	< 0.2 cm
d_z	< 0.5 cm	< 0.5 cm
Pixel hits	≥ 1	≥ 1
Tracker layers	≥ 8	≥ 8
σ_{p_T}/p_T	< 0.3	< 0.3
I_{rel}^{mod}	< 0.1	< 0.1

Table 3.4: Summary of the muon ID selection criteria.

361 3.3.2 Electron

362 Reconstruction

363 Text.

³⁶⁴ Bibliography

- 365 [1] ATLAS Collaboration. Observation of a new particle in the search for the Stan-
366 dard Model Higgs boson with the ATLAS detector at the LHC. *Phy. Lett. B*,
367 716:1, 2012.
- 368 [2] CMS Collaboration. Observation of a new boson at a mass of 125 GeV with the
369 CMS experiment at the LHC. *Phy. Lett. B*, 716:30, 2012.
- 370 [3] CMS Collaboration. Observation of a new boson with mass near 125 GeV in pp
371 collisions at $\sqrt{s} = 7$ and 8 TeV. *JHEP*, 06:081, 2013.
- 372 [4] CMS Collaboration. Precise determination of the mass of the Higgs boson and
373 tests of compatibility of its couplings with the standard model predictions using
374 proton collisions at 7 and 8 TeV. *Eur. Phys. J. C*, 75:212, 2015.
- 375 [5] ATLAS Collaboration. Measurement of the Higgs boson mass from the $H \rightarrow \gamma\gamma$
376 and $H \rightarrow ZZ^* \rightarrow 4l$ channels in pp collisions at center-of-mass energies of 7 and
377 8 TeV with the ATLAS detector. *Phys. Rev. D*, 90:052004, 2014.
- 378 [6] ATLAS Collaboration. Evidence for the spin-0 nature of the Higgs boson using
379 ATLAS data. *Phys. Lett. B*, 726:120, 2013.
- 380 [7] CMS and ATLAS Collaboration. Combined Measurement of the Higgs Boson
381 Mass in pp Collisions at $\sqrt{s} = 7$ and 8 TeV with the ATLAS and CMS Experi-
382 ments. *Phys. Rev. Lett.*, 114:191803, 2015.
- 383 [8] Mads T. Frandsen. Minimal Walking Technicolor. arXiv:0710.4333 [hep-ph],
384 <http://arxiv.org/abs/0710.4333>, 2007.
- 385 [9] T. Han, H. E. Logan, B. McElrath, and L.-T. Wang. Phenomenology of the little
386 Higgs model. *Phys. Rev. D*, 67:095004, 2003.
- 387 [10] M. Schmaltz and D. Tucker-Smith. LITTLE HIGGS THEORIES. *Annual Review*
388 of Nuclear and Particle Science, 55:no. 1, 229–270, 2005.
- 389 [11] M. Perelstein. Little Higgs models and their phenomenolog. *Progress in Particle*
390 and Neclear Physics, 58:no. 1, 247–291, 2007.
- 391 [12] R. Contino, D. Pappadopulo, D. Marzocca, and R. Rattazzi. On the effect of
392 resonances in composite Higgs phenomenology. *Journal of High Energy Physic*,
393 2011:no. 10, 1–50, 2011.

- 394 [13] D. Marzocca, M. Serone, and J. Shu. General composite Higgs model. *Journal*
 395 *of High Energy Physics*, 2012:no. 8, 1–52, 2012.
- 396 [14] B. Bellazzini, C. Csaki, and J. Serra. Composite Higgses. *Eur. Phys. J.*, C74:no.
 397 5, 2766, 2014.
- 398 [15] D. Pappadopulo, R. Torre A. Thamm, and A. Wulzer. Heavy vector triplets:
 399 bridging theory and data. *Journal of High Energy Physics*, 2014:no. 9, 1–50,
 400 2014.
- 401 [16] Andrea Wulzer. An Equivalent Gauge and the Equivalence Theorem.
 402 arXiv:1309.6055 [hep-ph], <http://arxiv.org/abs/1309.6055>, 2013.
- 403 [17] V. Barger, W.-Y. Keung, and E. Ma. Gauge model with light W and Z bosons.
 404 *Phys. Rev. D*, 22:727, 1980.
- 405 [18] Lisa Benato, Yu-Hsiang Chang, Ching-Wei Chen, Michele de Gruttola, Ra-
 406 manan Khurana Ji-Kong Huang, Stefano Lacaprara, Yun-Ju Lu, Jacopo Pazzini,
 407 Maurizio Pierini, Henry Yee-Shian Tong, Jun-Yi Wu, Shin-Shan Eiko Yu, Marco
 408 Zanetti, and Alberto Zucchetta. Search for heavy resonances decaying into a vec-
 409 tor boson and a higgs boson in the $(ll, l\nu, \nu\nu)b\bar{b}$ final state. CMS Note 2015/186,
 410 CMS, 2015.
- 411 [19] A. Benaglia. The CMS ECAL performance with examples. *JINST*, 09:C02008,
 412 2014.
- 413 [20] CMS HCAL Collaboration. Design, performance, and calibration of cms hadron-
 414 barrel calorimeter wedges. CMS Note 2006/138, CMS, 2006.
- 415 [21] Victor Daniel Elvira. Measurement of the pion energy response and resolution
 416 in the cms hcal test beam 2002 experiment. CMS Note 2004/020, CMS, 2004.
- 417 [22] J. Brooke on behalf of the CMS Collaboration. Performance of the CMS Level-1
 418 Trigger. arXiv:1302.2469 [hep-ex], <http://arxiv.org/abs/1302.2469>, 2013.
- 419 [23] J. Alwall, R. Frederix, S. Frixione, V. Hirschi, F. Maltoni, O. Mattelaer, H.-S.
 420 Shaoand T. Stelzer, P. Torrielli, and M. Zaro. The automated computation of
 421 tree-level and next-to-leading order differential cross sections, and their matching
 422 to parton shower simulations. *JHEP*, 07:079, 2014.
- 423 [24] Torbjorn Sjostrand, Stephen Mrenna, and Peter Skands. PYTHIA 6.4 Physics
 424 and Manual. *JHEP*, 0605:026, 2006.
- 425 [25] Stefano Frixione, Paolo Nason, and Giovanni Ridolfi. The POWHEG-hvq manual
 426 version 1.0. arXiv:0707.3081 [hep-ph], <http://arxiv.org/abs/0707.3081>, 2007.
- 427 [26] S. Chatrchyan et al. Performance of CMS muon reconstruction in pp collision
 428 events at $\sqrt{s} = 7$ TeV. *JINST*, 7:P10002, 2012.

- 429 [27] Wolfgang Adam, Boris Mangano, Thomas Speer, and Teddy Todorow. Track
430 reconstruction in the cms tracker. CMS Note 2006/041, CMS, 2006.
- 431 [28] CMS Collaboration. Baseline muon selections for Run-I.
432 <https://twiki.cern.ch/twiki/bin/view/CMSPublic/SWGuideMuonId>.